

# Offset free generalized model predictive control for 3-phase LCL-filter based grid-tied inverters

Hasan Zamani<sup>a,b,\*</sup>, Karim Abbaszadeh<sup>a</sup>, MohammadHadi Karimi<sup>a</sup>, Johan Gyselinck<sup>b</sup>

<sup>a</sup> K.N. Toosi University of Technology, Tehran, Iran

<sup>b</sup> Université Liber de Bruxelles, Brussels 1050, Belgium

## ARTICLE INFO

### Keywords:

Generalized model predictive control  
Steady state offset  
Natural reference frame  
Active damping  
Computation time

## ABSTRACT

This paper presents a Generalized Model Predictive Control (GPC) in the natural reference frame for a 3-phase LCL-filter based grid-tied inverter. The proposed controller can track the sinusoidal reference without steady-state phase and amplitude offsets. This is achieved by parameterizing the control law matrices with considering the future reference trajectory.

To cope with the LCL filter resonance, traditional controllers need a damping method. The proposed controller has inherent damping against the LCL filter resonance and extra sensors are avoided. The controller parameters are selected by a sensitivity analysis that guarantees the closed-loop stability.

The proposed controller provides high accuracy in controlling active and reactive currents, robustness against grid inductance variations, low real-time computation, and a fixed switching frequency. The simulation and experimental results prove the performance of the controller in tracking the grid-side reference currents.

## 1. Introduction

Grid-tied inverters play an important role in the power delivery from renewable energy sources to power grids and have attracted attention in recent years. An L or LCL filter is usually integrated at the AC side of the inverter to inject current with low Total Harmonic Distortion (THD). Switching harmonics attenuation of the LCL filter is higher, but it introduces two poles on the imaginary axis, which makes the closed-loop system unstable. The resonance damping techniques are mainly divided into Passive Damping (PD) and Active Damping (AD) [1–4]. PD techniques generate losses and are unsuitable, especially in high current applications. AD techniques require extra sensors, which increases the total cost. Therefore, the motivation is to design a controller with inherent robustness against the resonance that can fulfill grid requirements such as fast dynamic response, high bandwidth to reject disturbances, and robustness against model uncertainties. Modern control approaches such as Sliding Mode Control (SMC) [5,6], Deadbeat Predictive Control (DPC) [7], and state-feedback control have been proposed for the grid-tied inverters [8]. Basically, using these controllers does not eliminate the need for AD.

Continuous Control Set Model Predictive Control (CCS-MPC) as a model-based control method considers all the process interactions and

mitigates every harmonics around the resonant frequency, and thus eliminates the need for extra sensors for AD.

Model predictive controllers in power electronics can be divided into two groups. The first group proposes an algorithm to find the best switching states to minimize a cost function and is called Finite Control Set Model Predictive Control (FCS-MPC) [9–11]. FCS-MPC methods are flexible and robust but have some disadvantages. The current tracking error of this method is not as small as expected, because there is no integral error between the output and the reference [11]. Also, in applications with a higher number of switching states like multi-level inverters, the real-time computation increases dramatically [12–14]. Moreover, this method requires sensors to overcome the LCL filter resonance [15].

The second group is CCS-MPC. In this group, the control law is derived by solving an analytical optimization problem. All the optimization process is done offline and the result is programmed in a processor. Contrary to FCS-MPC, the CCS-MPC outputs are in the continuous space, and thus it works with a fixed switching frequency [16]. A well-known sub-group of CCS-MPC, which has been used in power electronics is Generalized model Predictive Control (GPC) [17]. In this method, the trajectory of the output is predicted by solving the Diophantine equation or the state-space equation [18–20]. In [18], GPC

\* Corresponding author at: K.N. Toosi University of Technology, Tehran, Iran.  
E-mail address: [H.zamani@email.kntu.ac.ir](mailto:H.zamani@email.kntu.ac.ir) (H. Zamani).

is designed to control an L-filter based grid-tied inverter that has a larger THD for the injected currents than an LCL filter.

In [19], GPC is designed for an LCL-filter based grid-tied inverter. The inverter-side currents are the control targets. In this paper robustness against the LCL filter resonance is guaranteed by adding a passive resistor in series with the capacitor of the LCL filter. In addition, the closed-loop system is stable against the resonance when controlling the inverter-side currents. Also, in [20], GPC is designed with an observer (Kalman filter) to control the inverter-side currents. This observer increases the control complexity and real-time computational effort.

In [22], GPC is designed to control the grid-side currents of a 4-leg inverter. In this article, stability against the LCL filter resonance is achieved via feedback of the capacitor voltages. Also, a part of optimization is done in the real-time, which needs a powerful processor. In [23], to suppress the LCL filter resonance, the capacitor voltages are added to the cost function. These AD approaches need extra voltage sensors.

As a summary, to overcome the issue of resonance in the relevant papers about the LCL filter based grid-tied inverters, which are controlled by GPC, their cost functions include some state variables, or the inverter-side currents are the control targets. The former needs extra sensors. The closed-loop system is stable when taking the inverter-side currents as the control targets [34]. However, this selection does not provide enough precision in the control of both the power factor and the waveform of the current injected into the grid [8,21].

In the aforementioned articles about GPC, the controller is designed in the stationary frame. Setting a DC value for the reference over the prediction and control horizons could generate steady-state phase and amplitude offsets [24,25]. In [26,27], to remove the offsets, GPC is designed in the synchronous frame. The model in the synchronous frame is complex, and the model order is high. In addition, there is a heavy cross-coupling between the quadrature axes [28].

In this work, GPC is designed to control an LCL-filter based grid-tied inverter in the natural frame. To control the power factor at the common coupling point with the grid precisely, the grid-side currents are selected as the control targets. In order to select the controller parameters, the process of deriving the closed-loop transfer function and the open-loop transfer function is explained. Then, a sensitivity analysis is performed for the parameter selection to obtain the highest stability margins. By analyzing these transfer functions, it is shown that the closed-loop poles stay inside the unity circle when the capacitance and inductances of the LCL filter vary in a reasonable range.

The control law in each sampling time is updated according to a sequence of the past output, a sequence of the past input, and the future reference trajectory. The first two terms guarantee the stability of the closed-loop system, and the third term removes steady-state offsets.

It is shown that GPC will fail to remove the steady-state errors if the reference trajectory is not taken into account over the control and prediction horizons. Indeed, by neglecting the future setpoints over these horizons, GPC suffers from the same problem as the proportional-integral controllers in tracking sinusoidal references [29].

A summary of the proposed control advantages is:

- The controller has inherent robustness against the LCL filter resonance and thus removes the need for PD, which produces losses, or AD, which increases the total cost of the system due to the need for extra sensors.
- By selecting the controller parameter with a sensitivity analysis over the open-loop transfer function, the closed-loop system shows sufficiently high stability margins. First, the formulation of the open-loop and closed-loop functions is given.
- The analysis of the closed-loop transfer function shows the stability of the closed-loop system against the LCL filter inductance and capacitance variations.
- The control law is parameterized based on the future reference trajectory over the control and prediction horizons to deal with the

steady-state offsets. The approach for the prediction of the future reference trajectory is discussed.

- The optimization routine is performed offline, and the control law can easily be implemented in a low-cost processor.
- To control the power factor precisely, the grid-side currents are selected as the control variables.

The remaining contents are organized as follow: in section 2, the dynamic model of the system is derived in the natural reference frame. In section 3, the theory behind the proposed controller, a detailed analysis of the closed-loop pole locations, synthesizing of future setpoints, and selection of GPC's parameters are explained. To verify the closed-loop performance and robustness of the controller, simulation and experimental results are given in 4 and 5, respectively. Finally, the conclusion is given in 6.

## 2. System modeling

Fig. 1 shows a 3-phase grid-tied inverter, and Table 1 lists the parameters under study. In this figure  $L_{a,b,c}^i$  are the inverter-side inductances,  $L_{abc}^g$  are the grid-side inductances and  $C_{a,b,c}$  are the capacitor elements of the LCL filter.  $r_l$  and  $r_c$  are parasitic equivalent series resistance (ESR) of the filter inductors and capacitors. In the following, it is assumed that data is acquired in discrete time and is available at sampling instants  $t = kT_s$ ,  $k = 1 \dots$ , with  $T_s$  the sample time.

Formulation of GPC requires the Controller Autoregressive Integrated Moving Average model (CARIMA). CARIMA is a standard description of systems in the discrete-time domain. The general form of the CARIMA model is [30]:

$$A(z^{-1})y(z^{-1}) = z^{-d}B(z^{-1})u(k-1) + C(z^{-1})\frac{e(z^{-1})}{\Delta} \quad (1)$$

with  $z^{-1}$  the backward Euler shift operator,  $d$  the input-output delay,  $y$  and  $u$  the output and input variables,  $e$  the variable that models the input noise,  $\Delta = 1 - z^{-1}$ . The A, B, C polynomials are:

$$A(z^{-1}) = 1 + a_1z^{-1} + a_2z^{-2} + \dots + a_{n_a}z^{-n_a} \quad (2)$$

$$B(z^{-1}) = b_0 + b_1z^{-1} + b_2z^{-2} + \dots + b_{n_b}z^{-n_b}$$

In the general case of white noise  $C(z^{-1})$  is assumed 1:

$$C(z^{-1}) = 1.$$

To obtain the CARIMA model, the dynamic system equations according to Fig. 1 in the natural frame are derived. A balanced 3-phase system is modeled, and hence transfer functions of all phases are identical. Dynamic equations of the phase leg a are:

$$v_a = r_l i_a^i + L_a^i \frac{di_a^i}{dt} + v_a^1 \quad (3)$$

$$v_a^1 = r_l i_a^g + L_a^g \frac{di_a^g}{dt} \quad (4)$$

$$i_a^c = C_a \frac{dv_a^c}{dt} \quad (5)$$

$$v_a^1 = v_a^c + r_c i_a^c \quad (6)$$

$$i_a^i = i_a^c + i_a^g \quad (7)$$

The i and g superscripts denote the inverter-side and the grid-side variables.  $v_a^1$  is the voltage across the capacitor filter and its parasitic resistance. In these equations, the grid voltage is assumed zero. It is shown in section 3.3 that adding a feedforward term of the grid voltage to the control's output compensates this simplification.

In the worst case where the parasitic resistances are neglected and



The recursive solutions for the  $E_j, F_j, G_j$  polynomials are [30]:

$$E_{j+1}(z^{-1}) = E_j(z^{-1}) + z^{-j}f_{j,0} \quad (17)$$

$$F_{j+1}(z^{-1}) = z[F_j(z^{-1}) - f_{j,0}\hat{A}(z^{-1})] \quad (18)$$

$$G_{j+1}(z^{-1}) = G_j(z^{-1}) + z^{-j}f_{j,0}B \quad (19)$$

with  $f_{j,0}$  the first coefficient of  $F_j$ . The initial values are:

$$E_0 = 1, F_1(z^{-1}) = z(1 - \hat{A}(z^{-1})). \quad (20)$$

The prediction equation in (16) includes both past and future signals. The matrix form of (16) that separates the past signals and future signals for  $j = 1$  to  $N$  is:

$$Y = G_f U + F Y_p + G_p U_p \quad (21)$$

with

$$Y = [\hat{y}(k+1) \quad \hat{y}(k+2) \quad \dots \quad \hat{y}(k+N)]^T \quad (22)$$

$$Y_p = [y(k) \quad y(k-1) \quad \dots \quad y(k-n_a)]^T$$

$$U = [\Delta u(k) \quad \Delta u(k+1) \quad \dots \quad \Delta u(k+N-1)]^T$$

$$U_p = [\Delta u(k-1) \quad \Delta u(k-2) \quad \dots \quad \Delta u(k-n_b)]^T$$

$$G_f = \begin{bmatrix} g_{0,0} & 0 & \dots & 0 \\ g_{1,1} & g_{1,0} & \dots & 0 \\ \vdots & \vdots & \vdots & \vdots \\ g_{N-1,N-1} & g_{N-1,N-2} & \dots & g_{N-1,0} \end{bmatrix} \cdot G_p$$

$$= \begin{bmatrix} g_{0,1} & \dots & g_{0,n_b-1} \\ g_{1,2} & \dots & g_{1,n_b} \\ \vdots & \vdots & \vdots \\ g_{N-1,N-1} & \dots & g_{N-1,n_b+N-1} \end{bmatrix}$$

with  $g_{j,i}$  the  $i^{\text{th}}$  coefficient of  $G_j$ .  $F Y_p + G_p U_p$  in (21) only depends on the past and is called the free response.

(21) can be rewritten as:

$$Y = G_f U + f \quad (23)$$

with  $f = F Y_p + G_p U_p$ . The matrix form of the cost function in terms of the control signals, which is derived by using (23) in (13), is:

$$J = (G_f U + f - W)^T (G_f U + f - W) + \lambda U^T U \quad (24)$$

with  $W$  the vector of the future setpoints over the interval  $N$ :

$$W = [w(k+1) \quad w(k+2) \quad \dots \quad w(k+N)]^T. \quad (25)$$

Setting the derivative of  $J$  with respect to  $U$  to zero, the control law is obtained:

$$U = (G_f^T G_f + \lambda I)^{-1} G_f^T (W - f). \quad (26)$$

with  $I$  the identity matrix.  $U$  is a vector that includes future control signals. In each sampling time, just  $\Delta u(k)$  is selected and applied to the process:

$$\Delta u(k) = K(W - f) \quad (27)$$

with  $K$  the first row of  $(G_f^T G_f + \lambda I)^{-1} G_f^T$ .

### 3.2. Closed-loop and open-loop relationships

Once the control law is derived, it is possible to obtain the closed-loop poles. Using  $f = F Y_p + G_p U_p$  in (27) results in:

$$\Delta u(k) = KW - Kf = KW - KFY_p - KG_p U_p \quad (28)$$

$KG_p U_p$  and  $KFY_p$  can be written as:

$$\begin{aligned} KG_p U_p &= K_u(z^{-1})\Delta u(k-1), \\ KFY_p &= K_y(z^{-1})y(k) \end{aligned} \quad (29)$$

with  $K_u$  and  $K_y$  the following polynomials:

$$K_u(z^{-1}) = \sum_{i=0}^{N-1} K_i g_{pi,0} + z^{-1} \sum_{i=0}^{N-1} K_i g_{pi,1} + \dots + z^{-n_b+1} \sum_{i=0}^{N-1} K_i g_{pi,n_b}$$

$$K_y = \sum_{i=0}^{N-1} K_i f_{i,0} + z^{-1} \sum_{i=0}^{N-1} K_i f_{i,1} + \dots + z^{-n_a} \sum_{i=0}^{N-1} K_i f_{i,n_a}$$

with  $g_{pi,j}$  the  $i^{\text{th}}$  column and  $j^{\text{th}}$  row element of  $G_p$ ,  $K_i$  the  $i^{\text{th}}$  element of  $K$ . Using (29) in (28) and rearranging (28) yields:

$$(1 + z^{-1}k_u(z^{-1}))\Delta u(k) = KW - K_y(z^{-1})y(k). \quad (30)$$

The future reference trajectory does not affect the closed-loop characteristic equation. For the stability analysis, the reference setpoints over the horizon  $N$  are kept constant ( $w(k+j) = w(k)$ ) and the  $KW$  becomes:

$$r = KW = w(k) \sum_{i=0}^{N-1} K(i)$$

with this assumption (30) is rewritten as:

$$\begin{aligned} \Delta u(k) &= (1 + z^{-1}k_u(z^{-1}))^{-1}r - (1 + z^{-1}k_u(z^{-1}))^{-1}k_y(z^{-1})y(k) \\ &= T_1(z^{-1})r - T_2(z^{-1})y(k) \end{aligned} \quad (31)$$

with  $T_1(z^{-1})$  and  $T_2(z^{-1})$  given by:

$$T_1(z^{-1}) = (1 + z^{-1}k_u(z^{-1}))^{-1}, T_2(z^{-1}) = (1 + z^{-1}k_u(z^{-1}))^{-1}k_y(z^{-1}).$$

Using (31) in (1) leads to:

$$A(z^{-1})\Delta y(k) = B(z^{-1})z^{-1}(T_1(z^{-1})r - T_2(z^{-1})y(k)). \quad (32)$$

Finally, the closed-loop transfer function relating  $y$  and  $r$  is obtained:

$$G_c(z^{-1}) = \frac{y(k)}{r} = (A(z^{-1})\Delta + B(z^{-1})z^{-1}T_2(z^{-1}))^{-1}B(z^{-1})z^{-1}T_1(z^{-1}). \quad (33)$$

The denominator of (33) is the characteristic equation, which determines the location of closed-loop poles.

In the next section, controller parameters are selected based on the stability analysis of the open-loop transfer function ( $G(z^{-1})$ ).  $G(z^{-1})$  is derived by defining  $err(k) = r - y(k)$  as the input and  $y(k)$  as the output. A cross multiplication between the first term and the second term of (33) yields:

$$y = G_c r$$

and  $r - y(k)$  becomes:

$$r - y(k) = r - G_c(z^{-1})r = (1 - G_c(z^{-1}))r = \frac{(1 - G_c(z^{-1}))}{G_c(z^{-1})}y(k)$$

Finally,  $G(z^{-1})$  is:

$$G(z^{-1}) = \frac{y(k)}{r - y(k)} = \frac{G_c(z^{-1})}{1 - G_c(z^{-1})}. \quad (34)$$

### 3.3. References synthesizing and the grid impact compensation

A Phase-Locked Loop (PLL) is a common technique for synchronization of grid-tied power converters. By setting the q-axis voltage to zero, the PLL output [03B8](k) is locked on the a-phase grid voltages. To control the active and reactive power, first the references of the grid-side currents are synthesized in the dq frame. Then, they are converted to the Cartesian frame and the amplitude and phase of the reference currents

$(I_{ref}, \theta_{ref})$  at the time instance  $k$  are determined. The space vector of the dq currents in the synchronous frame is:

$$\vec{i}_{ref} = i_{d,ref}^g + j i_{q,ref}^g = I_{ref} e^{j\theta_{ref}} \quad (35)$$

with  $i_{d,ref}^g$  and  $i_{q,ref}^g$  the dq reference currents,  $I_{ref}$  and  $\theta_{ref}$  given by:

$$I_{ref}(k) = \sqrt{i_{q,ref}^{g2} + i_{d,ref}^{g2}} \quad (36)$$

$$\theta_{ref}(k) = \arctan\left(\frac{i_{d,ref}^g}{i_{q,ref}^g}\right) \quad (37)$$

$i_{d,ref}^g$  controls the active power and  $i_{q,ref}^g$  controls the reactive power.  $\theta_{ref}(k)$  and  $\theta$  are added to determine the angle of the a-phase currents in the natural frame.  $I_{ref}(k)$  and  $\theta_{ref}(k)$  are constant as long as the quadrature reference currents are constant. But evolution of  $\theta$  (the PLL's output) should be taken into consideration over the predictive horizon  $N$ . The prediction value of  $\theta$  at time  $k+i$  is:

$$\theta(k+i) = \theta(k) + i2\pi f T_s \quad (38)$$

with  $f$  the fundamental utilized frequency. The a-phase reference current at  $t = k+i$  is:

$$w_a(k+i) = I_{ref} \sin(\theta(k+i) + \theta_{ref}(k)) = I_{ref} \sin(\theta(k) + i2\pi f T_s + \theta_{ref}(k)).$$

Finally,  $KW$  in (27) for the 3-phase currents becomes:

$$KW_a = I_{ref} \sum_{i=1}^N K(i) \sin(\theta(k) + \theta_{ref}(k) + i2\pi f T_s) \quad (39)$$

$$KW_b = I_{ref} \sum_{i=1}^N K(i) \sin\left(\theta(k) + \theta_{ref}(k) + i2\pi f T_s - \frac{2\pi}{3}\right)$$

$$KW_c = I_{ref} \sum_{i=1}^N K(i) \sin\left(\theta(k) + \theta_{ref}(k) + i2\pi f T_s + \frac{2\pi}{3}\right)$$

The grid voltage harmonics can distort the injected currents. Adding a feedforward term of the grid voltage to the controller's output reduces this distortion. According to the superposition theorem, the grid-side current can be written as:

$$i_g = G_L u_c|_{u_g=0} - G_L u_g|_{u_c=0} \quad (40)$$

with  $G_L = 1/L_s$  and  $L$  the sum of grid-side and inverter-side inductances:  $L = L_s^g + L_a^i$ ,  $u_g$  and  $u_c$  the grid voltage and the controller output, respectively. To obtain (40), the LCL filter is approximated by an L filter. This assumption is valid below the resonance frequency [20]. Adding the feed-forward term to the controller' output yields:

$$i_g = G_L(u_c + u_g) - G_L u_g = G_L u_c. \quad (41)$$

(41) shows that the injected current does not depend on the grid voltage and thus its harmonics anymore. This is an advantage usage of GPC over FCS-MPC in which the CCS-MPC's control law ( $u_c$ ) can be modified. FCS-MPC needs some modifications in the cost function to reduce the impact of the grid voltage harmonics, which increase the real-time computation time.

### 3.4. Selection of the controller's parameters

$N$ , and  $\lambda$  play an important role in the stability of the closed-loop system. To determine the value of these parameters, the future set-points over the interval  $N$  are kept constant and the Phase Margin (PM) and Gain Margin (GM) of  $G(z^{-1})$  in (34) are studied. It is important to notice that equations in (39) are synthesized in real-time and real-time computation increases with  $N$ . Therefore, the goal is to find the maximum value of GM and PM for the lowest value of  $N$ . Figs. 2 and 3

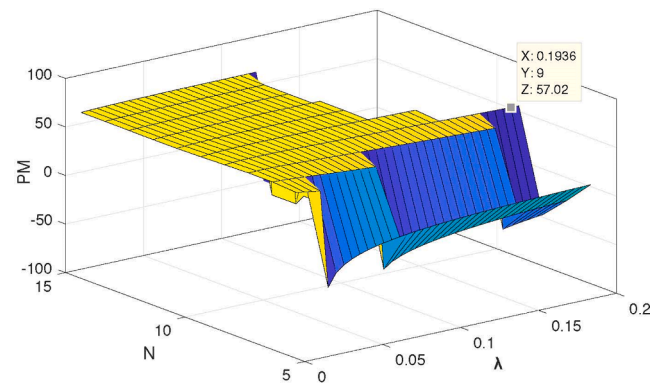


Fig. 2. PM of the open loop transfer function for variations of  $N$  between 5 and 15, and  $\lambda$  between 0.01 and 0.2.

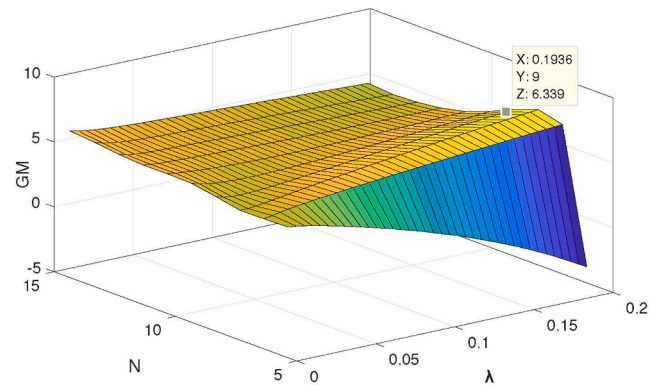


Fig. 3. GM of the open loop transfer function for variations of  $N$  between 5 and 15, and  $\lambda$  between 0.01 and 0.2.

show the PM and GM respectively. In these figures,  $N$  changes in the interval of [5 15], and  $\lambda$  changes in the interval of [0.01 0.2].

According to Figs. 2 and 3, the set of  $N = 9$  and  $\lambda = 0.1936$  corresponds to the lowest value of  $N$  that generates the highest values of PM and GM. The values of PM and GM for this selection is  $57^\circ$  and 6.4 dB. The control law and the  $G(z^{-1})$  transfer function for the selected parameters are:

$$\Delta u(k) = -K_u \Delta u(k-1) - K_y y(k) + K_w [w(k+1), \dots, w(k+9)]^T \quad (42)$$

$$k_u(z^{-1}) = 0.4108 + 0.0867z^{-1}$$

$$k_y(z^{-1}) = 130.134 - 3336.814z^{-1} + 322.042z^{-2} - 111.007z^{-3}$$

$$k_w = [1.54 \ 10.95 \ 30.08 \ 54.66 \ 76.78 \ 88.24 \ 83.56 \ 61.95 \ 27.69] \times 10^{-2}$$

$$G(z^{-1}) = 10^{-3} \times \frac{1.734z^{-1} + 6.82z^{-2} + 1.735z^{-3}}{1 - 3.403z^{-1} + 4.641z^{-2} - 3.003z^{-3} + 0.7653z^{-4}}. \quad (43)$$

The control law in (42) includes a sequence of the past output and the past input with  $K_y(z^{-1})$  and  $K_u(z^{-1})$  polynomials, respectively. The orders of  $K_y(z^{-1})$  and the model's denominator ( $A(z^{-1})$  in (12)) are equal. Also, the orders of  $K_u(z^{-1})$  and the model's numerator ( $B(z^{-1})$  in (12)) are in agreement. This shows that the proposed controller considers all the interactions of the system and does not allow harmonics around the LCL filter resonance frequency pass through the LCL filter and hence provides robustness against the LCL filter resonance.

Fig. 4 shows the Bode diagrams of  $G_{sys}(s)$  in (8) and  $G(z^{-1})$  in (43). There is a peak in the magnitude of  $G_{sys}(s)$  at the resonance frequency

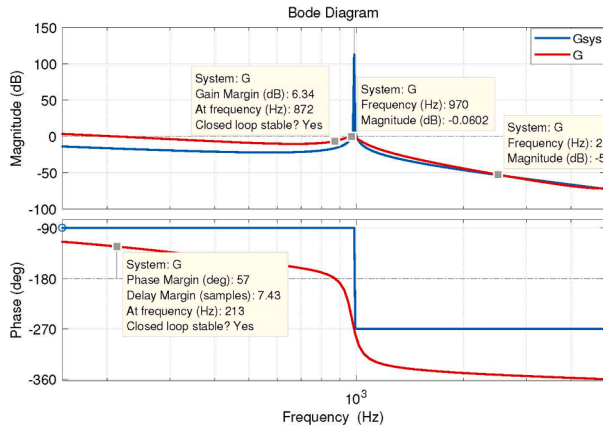


Fig. 4. The Bode diagrams of  $G_{sys}(s)$  and  $G(z^{-1})$ , the LCL filter resonance is damped in  $G(z^{-1})$  and the closed-loop system is stable.

while the phase crosses  $-180^\circ$ . According to the Nyquist theorem, the closed-loop system is unstable [33]. The Bode diagram of  $G(z^{-1})$  shows that the LCL filter resonance peak is damped. It is marked at 970 Hz. The obtained GM and PM that are marked in this figure shows that the controller restrains the resonance effectively and the closed-loop system is stable. This figure also shows that the magnitude of two transfer functions for the frequencies above 2.5 kHz are overlapped. Therefore, the controller does not affect the LCL filter ability in attenuation of switching harmonics that are centred on 10 kHz and its multiples.

In addition, the low-frequency gain of  $G(z^{-1})$  is higher than  $G_{sys}(s)$ , which means better usage of the DC link and better performance of tracking signals by the proposed method.

To study the system stability against parameter variations of the LCL filter elements, two sensitivity analyses are performed. The pole-zero map of the closed-loop system for variations of the grid-side inductance and capacitance are shown in Figs. 5 and 6, respectively. The inductance varies between 1.5 mH and 3 mH, and the capacitance varies between 17  $\mu$ F and 22  $\mu$ F. Despite of these variations all poles are inside the unity circuit and the closed-loop system is stable. The same result, which is given in Fig. 5 is valid for variations of the inverter-side inductance, because  $G_{sys}(s)$  is symmetrical for  $L_1$  and  $L_2$ .

For a comparative analysis, GPC and a PI controller are compared. The coefficients of the PI controller are tuned using the symmetrical optimum method [32]:

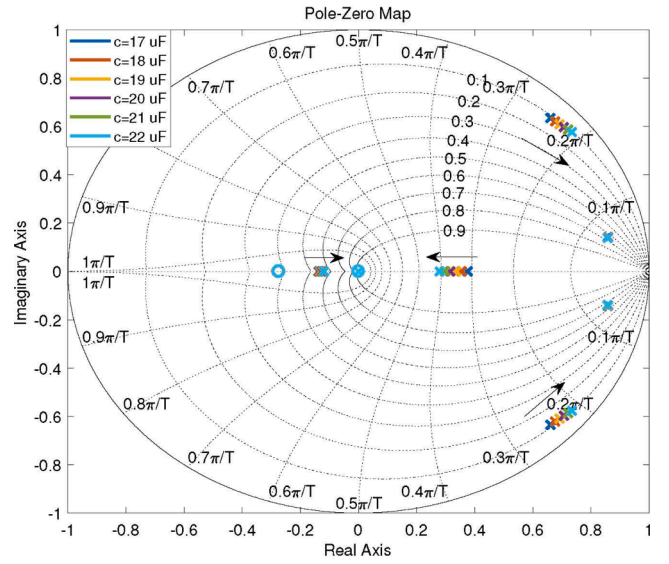


Fig. 6. Pole-zero map when  $C$  varies between 17  $\mu$ F and 22  $\mu$ F, despite of the capacitance variations, all closed-loop poles stay inside the unity circle.

$$K_p = \frac{L_1 + L_2}{2T_s}, T_i = a^2 T_s, a = 3 \quad (44)$$

with  $a$  the parameter for setting the cross-over frequency,  $T_s$  the sampling time,  $K_p$  the proportional gain,  $T_i$  the time constant of the integral part of the PI controller with the following transfer function:

$$G_{PI}(s) = \frac{K_p(sT_i + 1)}{sT_i} \quad (45)$$

Fig. 7 shows the Bode diagrams of three systems. In this figure,  $G_1$  (the dash-black curve) is the cascaded transfer function of  $G_{sys}$  and  $G_{PI}$  without AD,  $G_2$  (the red curve) is the cascaded transfer function with AD (the capacitor's currents with a tuned gain are added to the PI controller's output), and  $G$  (the blue curve) is introduced in (34) (the open-loop transfer function in the presence of GPC). This figure shows that the closed-loop system of  $G_1$  is unstable, because the phase crosses  $-180^\circ$  while the magnitude is above 0 dB, the closed-loop system of  $G_2$  is stable but this method needs extra sensors for measuring the capacitor's

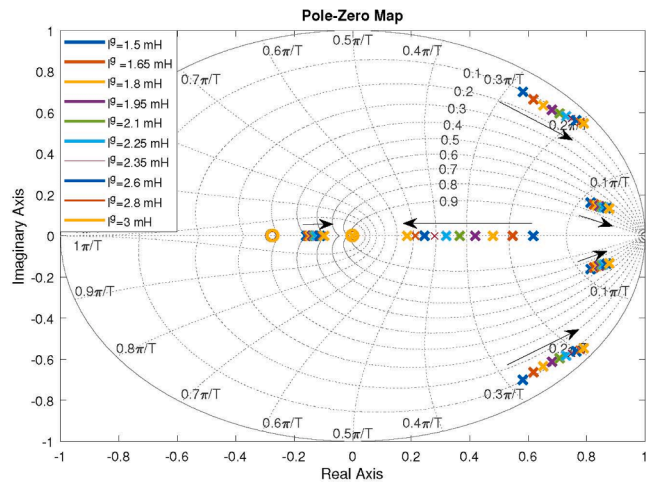


Fig. 5. Pole-zero map when  $L^s$  varies between 1.5 mH and 3 mH, despite of the inductance variations, all closed-loop poles stay inside the unity circle.

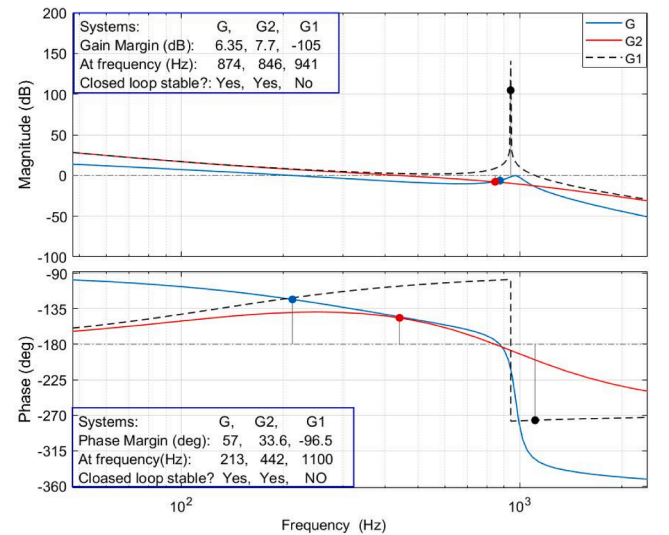


Fig. 7. The Bode diagrams of the open-loop system in presence of the PI controller without AD (dash-black curve), the PI controller with AD (red curve), and the GPC (blue curve).

currents, and  $G$  shows inherent robustness against the LCL filter resonance. In addition, comparing high-frequency gains of the stable PI controller and GPC shows that the attenuation of switching harmonics of GPC is higher because its gain reduction is sharper. PMs and GMs of these systems are summarized in Table 2. The PM of GPC is much higher than the stable PI controller, and the GM of the PI controller is a bit higher.

#### 4. Simulation results

The entire system, including the inverter, SVM, and GPC is simulated in MATLAB/Simulink for the control performance validation. The simulation parameter values are listed in Table 1. Synthesizing the reference currents are.

are explained in section 3.3. The controller performance is evaluated in the following items:

##### 4.1. Step reference

Fig. 8 shows the transient behavior against the reference changes. In this simulation, the d-axis reference current is stepped up from 3 A to 6 A at  $t = 0.1$  s. The q-axis reference current is kept at zero. The settling time is less than 3 ms and the overshoot and oscillation are negligible.

##### 4.2. Future reference trajectory and the grid voltage feed-forward term

$i1_a^g$  in Fig. 9 shows that the controller tracks the reference without any offsets in the amplitude and phase. This is achieved when  $W$  in (25) is parameterized with considering the future reference trajectory over the control horizon.

In the next test, a DC value is set for the reference trajectory during the whole interval of  $N$ .  $i2_a^g$  in Fig. 9 shows the result. The phase error between the reference current and the grid-side current is obvious.

The influence of parameterizing  $W$  is evaluated over THD of the injected current (THDi). Fig. 10 shows the 3-phase grid voltages and the grid-side currents. Fig. 11 and Fig. 12 show their frequency spectrum. THD of the grid voltage (THDv) is 9.68% and the obtained THDi is 2.94%, which meets the grid standards [18].

The amplitude of the current harmonic at the resonance frequency, which is marked in Fig. 12 is 0.11 % relative to the fundamental frequency. This shows that the proposed controller has damped the LCL filter resonance effectively. Fig. 13 shows the injected current and its reference in this test. Again, there is no offset in the amplitude and the phase of the injected current.

The simulation is repeated by neglecting the future reference trajectory over the interval  $N$ . Also, the grid voltage feed-forward term is not used. Fig. 14 shows that the current is distorted and the steady-state phase offset appears. Fig. 15 shows the frequency spectrum of the current. THDi has increased to 14.55%, which is not acceptable anymore.

##### Grid impedance variation and disturbance rejection

The proposed controller is tested under a grid-side inductance variation, which occurs in a weak grid. The grid-side inductances are stepped up from 1.5 mH to 3.5 mH at  $t = 0.05$  s and is backed to 1.5 mH at  $t = 0.1$  s. Fig. 16 shows the results. The controller has coped with the variations successfully.

The controller can also operate in the case of a grid voltage dip. A voltage dip is a disturbance that the RMS value of the line voltage is reduced for less than 500 ms [6]. A grid voltage dip of 10% is applied at

**Table 2**  
Comparative Analysis.

Algorithm	PM	GM	Is closed loop stable?
The PI control without AD	-95.5	-105	No
The PI control wit AD	33.6	7.7	Yes
GPC	57	6.35	Yes

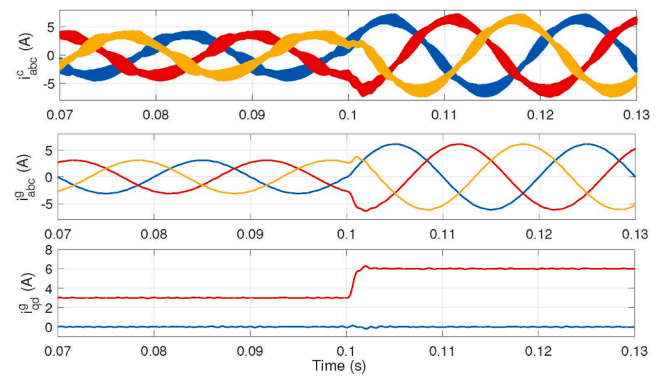


**Fig. 8.** The transient response, the d-axis reference current is stepped up at  $t = 0.1$  s from 3 A to 6 A, the q-axis reference current is kept at 0 A.

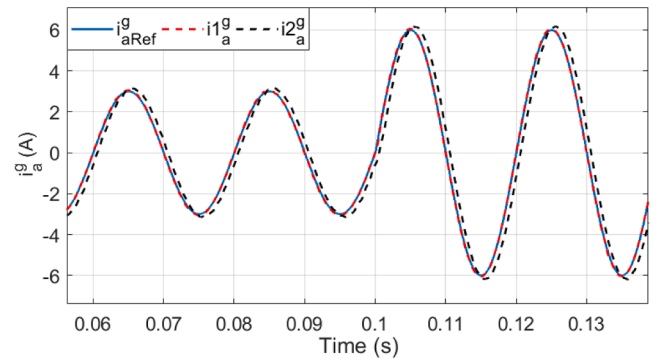


**Fig. 9.** The a-phase grid-side currents and its reference,  $i1_a^g$  is obtained with considering the future reference trajectory over the control horizon and  $i2_a^g$  is obtained with stteing a DC value for the reference in this horizon, the phase offset is observed in  $i2_a^g$ .

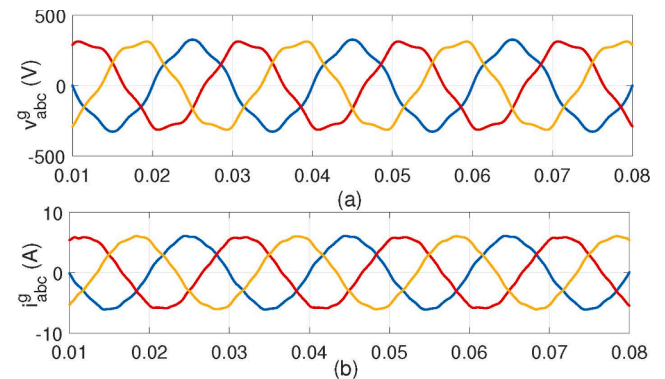


**Fig. 10.** The grid voltages are distorted: (a) the grid voltages, THDv = 9.68%, (b) the grid-side currents, THDi = 2.94%.

= 0.05 s. Fig. 17 shows the results. The controller is observed to deal with this disturbance in less than 10 ms and the currents follow their references accurately.

The next simulation evaluates the ability of the controller to reject disturbances whose harmonics are around the resonance frequency [21]. In this simulation, a 10  $V_{rms}$  harmonic with the frequency of the LCL filter resonance is added to the grid voltages. Fig. 18 shows the 3-phase grid currents. The currents are distorted, but the system is stable.

#### 5. Experimental results

The performances of the proposed controller are evaluated in a

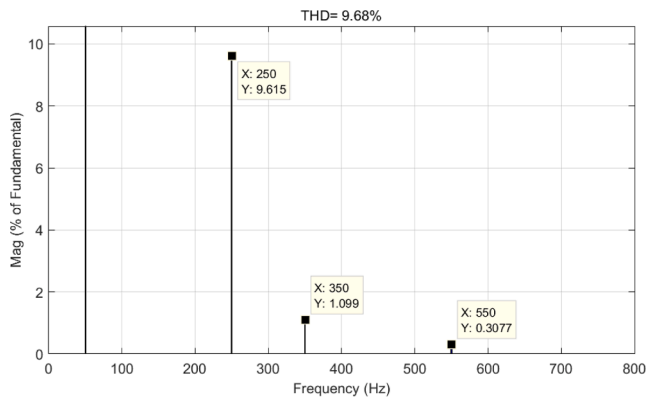


Fig. 11. The a-phase grid voltage spectrum, the grid voltages are distorted and THDv is 9.68 %.

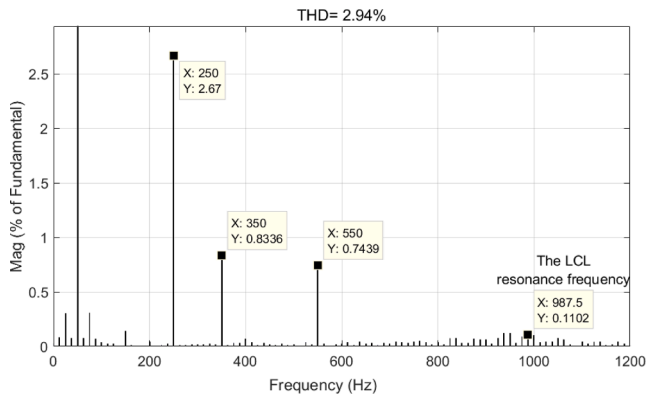


Fig. 12. The frequency spectrum corresponding to the injected current, the feed-forward term and future reference trajectory over the interval  $N$  are considered.

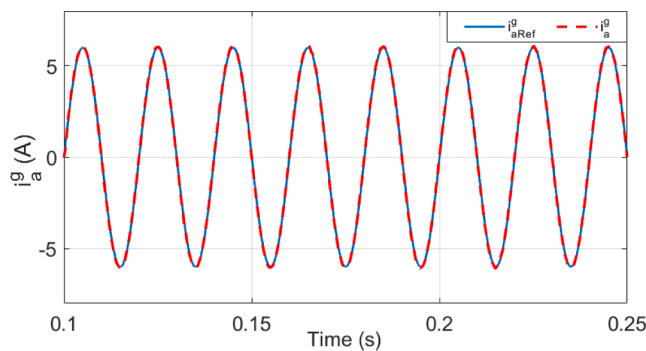


Fig. 13. The a-phase grid-side current ( $i_a^g$ ) and its reference ( $i_{aRef}^g$ ), THDv is 9.68 % and THDi is 2.94 %.

voltage source inverter connected to a 3-phase, 20 Amp, 380-volts transformer. The grid-side inductances are 3.3 mH with 5% tolerance. The filter's capacitances are 20  $\mu$ F. The GPC coefficients are tuned for a 2.3 mH grid-side inductance. This intentional difference examines the robustness of the proposed controller for grid inductance variations. The control algorithm is implemented into adSPACE 1103 fast prototype interface. Figs. 19 and 20 show the test-bench and the control unit block diagram, respectively.

The computation time is an evaluation criterion of a control algorithm. To determine the computation time of different parts, a digital output pin was set high at the start point of each algorithm, and it was set down when the algorithm was evaluated. This test was done in

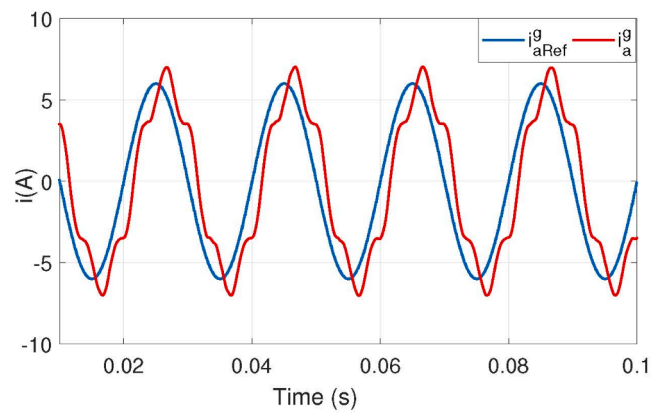


Fig. 14. The a-phase grid-side current (red line) and its reference (blue line) when the future reference trajectory is neglected and the grid voltage feed-forward term is not used.

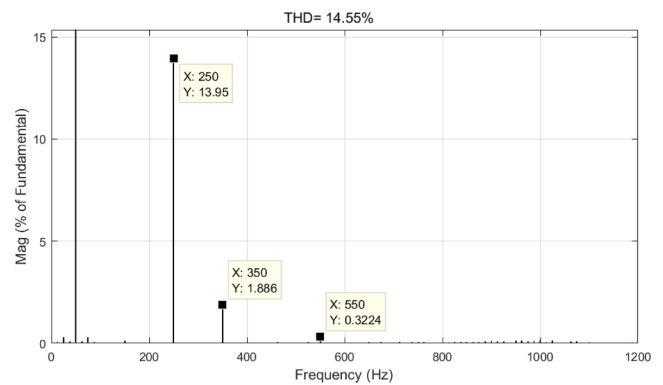


Fig. 15. The frequency spectrum corresponding to the a-phase grid-side current, the future reference trajectory is neglected and the grid voltage feed-forward term is not used.

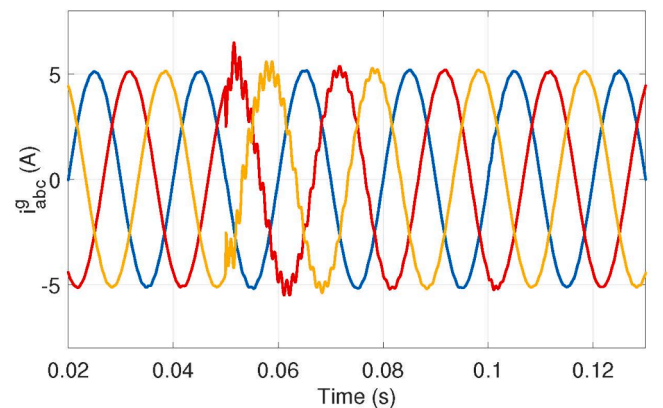


Fig. 16. The grid-side inductances are stepped up from 1.5 mH to 3.5 mH att = 0.05 s and is backed into 1.5 mH att = 0.1 s.

STM32407ZE microcontroller.

Fig. 21 and Table 3 show the computation time of the total control algorithm, the reference synthesizing algorithm, and the GPC algorithm. Considerably, the most computation time of GPC is devoted for synthesizing the 3-phase current references, which is 9  $\mu$ s. The total computation time is about 35  $\mu$ s, and the CPU utilization is about 35%. The low computation time was expected because the optimization of GPC is performed offline, and some simple numerical expression is



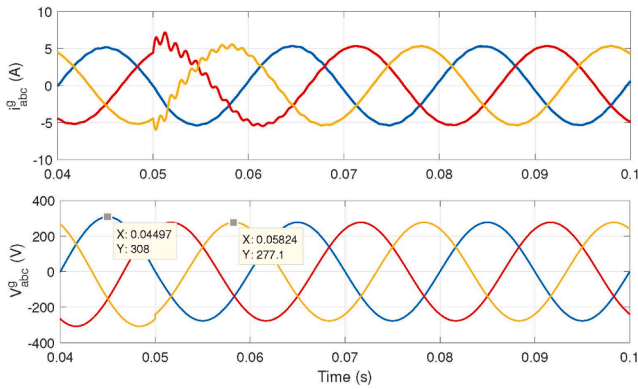


Fig. 17. The Performance of the proposed controller against the grid voltage dip: a 3-phase grid voltage dip of 10% is applied at  $t = 0.05$  s.

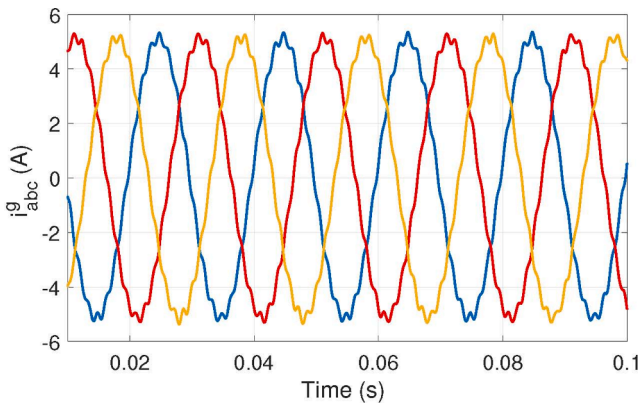


Fig. 18. The 3-phase grid currents when the grid voltages include a harmonic with the frequency of the LCL filter resonance.

executed in real-time. Therefore, the proposed controller can be easily implemented and does not require a powerful or dual co-processor [22].

Fig. 22 shows the steady-state experimental results of the grid-side currents in the natural frame together with the d-axis current, the d and q reference currents are set to 7 A, 0 A, respectively. The currents in the synchronous and natural frames follow their references.

The difference between the experimental results and the simulation results is due to nonlinearity in the components, particularly the inductances of the LCL filter, and the nonlinearity in the inverter. Also,

harmonics in the grid voltages affect the PLL output, and so affect the injected currents.

Fig. 23 shows the a-phase grid voltage and current, simultaneously. The aim is to study the grid voltages feedforward term and the reference trajectory effects over the interval  $N$ .

Fig. 23 (a) shows that there is a phase offset between the grid voltage and the injected current when the evolution of the reference over the interval  $N$  isn't considered and the feedforward term isn't used. Fig. 23 (b) shows that the offset disappears when these two terms are considered. A THDi of 3% is obtained in this experiment, which is in accordance with IEEE Std. 1547–2018 standard. This test ensures the controller's ability to inject current with unity power factor, which is important in the normal operation.

The capability of controllers to inject reactive current is important during fault conditions for assisting and improving the grid's stability. Fig. 24 shows the injected currents in the stationary and synchronous frames. Both d and q reference currents are set to 5 A. It can also be seen that the dq currents are well tracked by the proposed controller.

To evaluate the transient performance of the controller, the d-axis reference current is stepped up from 2.5 A to 7 A. The q-axis reference current is 0 A. Fig. 25 shows the grid-side currents together with the dq current. The controller shows a fast dynamic response and the settling time is less than 6 ms.

In the next test, the q-axis reference current is stepped down from 6 A to 2.5 A while the d-axis reference current is set to 1 A. Fig. 26 shows the results. In both tests of the step changes, the reference is tracked well. In addition, the controller's inherent damping against the LCL filter resonance is obvious as there is no oscillation in the currents.

Fig. 27 shows the controller performance under a 4.8 % symmetrical grid voltage dip. The currents follow their references without any change.

The next tests analyze the future reference trajectory effect as well as the feed-forward term. In these tests, the reference values for both axes are 5 A. Fig. 28 (a) shows the dq currents where the future reference trajectory is not taken into account over the interval  $N$ . The offsets over the d and q axes are around 0.65 A and  $-0.7$  A, respectively.

Fig. 28 (b) shows the currents where both the future reference trajectory and the feedforward term are neglected. The offsets in the d and q currents are around 0.8 A and  $-3.1$  A. Therefore, parametrizing the  $W$  matrix with considering setpoints over the interval  $N$ , and using the feedforward term remove the steady-state offset and the injected active and reactive power are controlled more precisely.

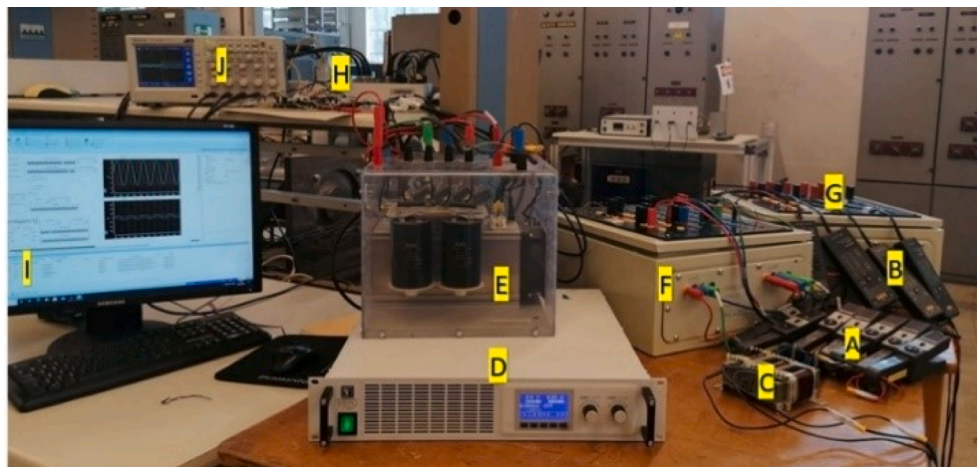


Fig. 19. The laboratory test bench with (A) current sensors, (B) voltage sensors, (C) extra grid-side inductors, (D) DC power supply, (E) inverter, (F) inverter-side and grid-side inductors, (G) AC capacitors, (H) dSPACE 1103, (J) oscilloscope, (I) ControlDesk software.

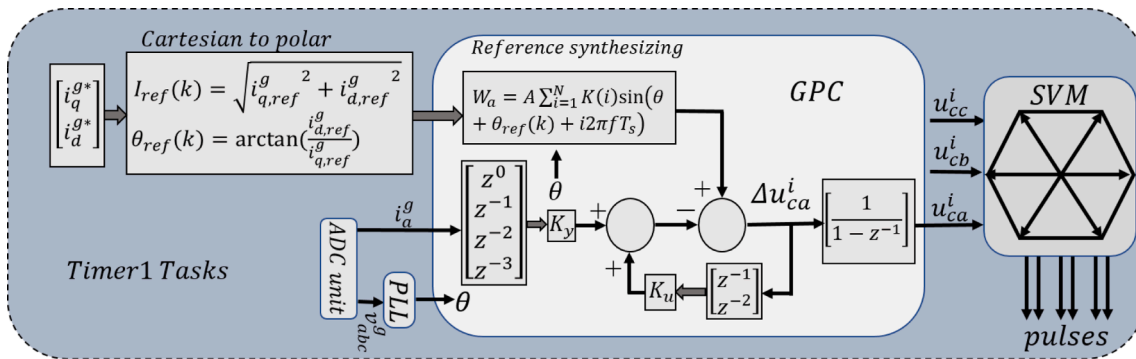


Fig. 20. Overall control unit implemented in dSPACE 1103 prototype.

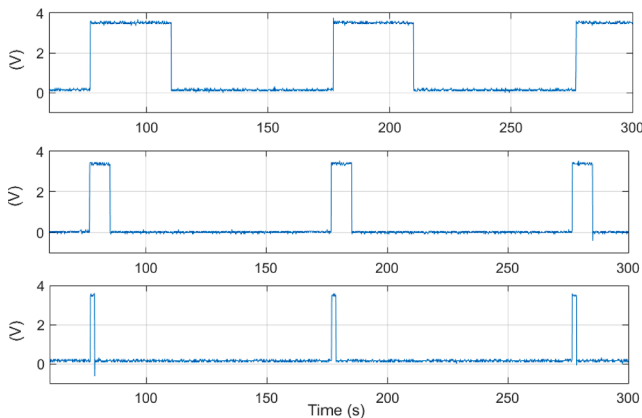


Fig. 21. Computation time, (a) Total algorithm computation time, (b) reference synthesizing computation time, (c) GPC computation time.

Table 3  
Computation Time.

Algorithm	Time ( $\mu$ s)
GPC	1.7
Reference synthesizing	9.0
ADC + SVM	23.0
Other parts	1.2

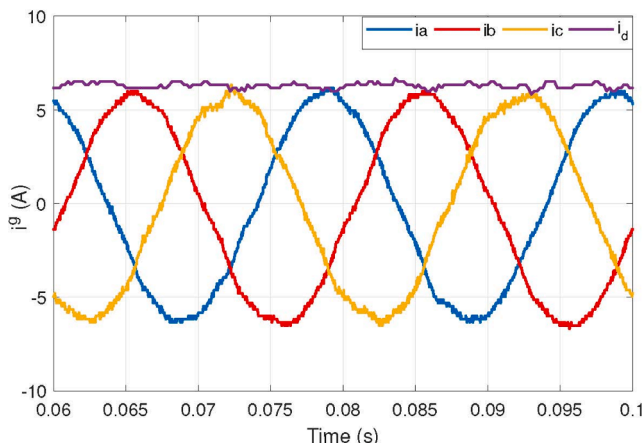


Fig. 22. The steady state response of GPC.

6. Conclusion

In this paper, GPC for controlling the grid-side currents of an LCL-filter based grid-tied inverter was proposed. The controller was

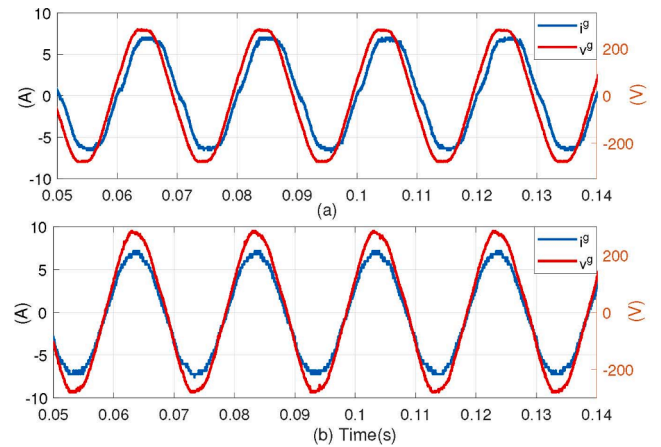


Fig. 23. The a-phase grid voltage (red lines) and the injected current (blue lines). (a) without considering the future reference trajectory and feed-forward term, (b) with considering these two terms, the dq reference currents are 7 A and 0 A.

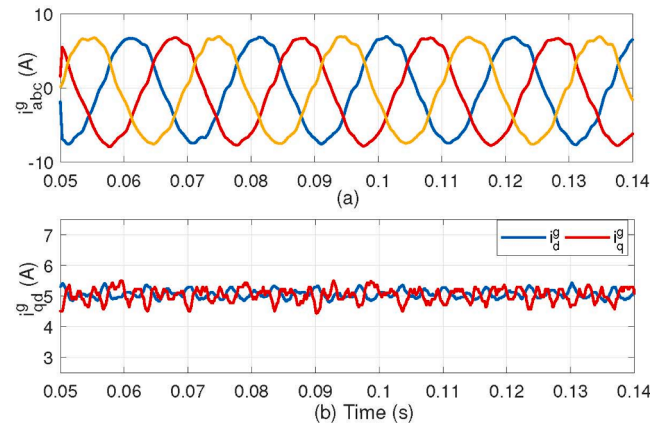


Fig. 24. The grid-side currents in the synchronous and stationary frame when the active and reactive reference currents are both set at 5 A.

designed in the natural frame where the references are sinusoidal. To track the sinusoidal reference, the control law over the control horizon was parameterized based on the future reference trajectory.

The proposed controller showed inherent robustness against the LCL filter resonance and extra sensor was avoided. The parameters of the controller were selected to provide the highest possible value of GM and PM. The obtained PM and GM imply a robust system.

To examine the controller performance against the grid-inductance change, which happens usually in a weak grid, the experimental results were obtained with an inductance about 1.5 times higher than the

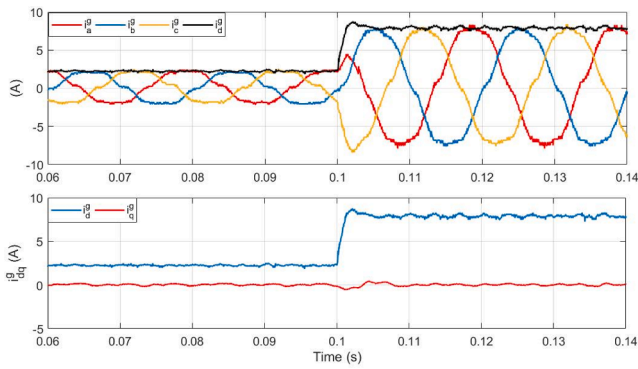


Fig. 25. The d-axis reference current is stepped up at  $t = 0.1$  s from 2.5 A to 7 A, the q-axis current is set to 0 A.

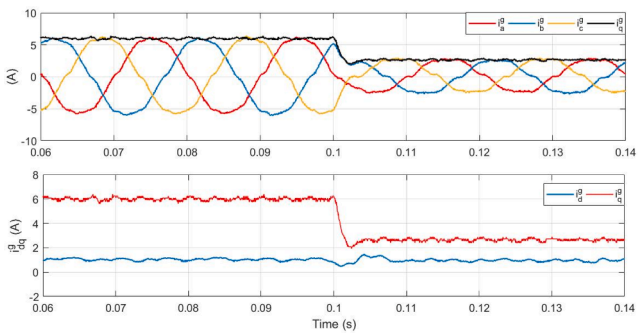


Fig. 26. The q-axis reference current step is stepped down at  $t = 0.1$  s from 6 A to 2.5 A.

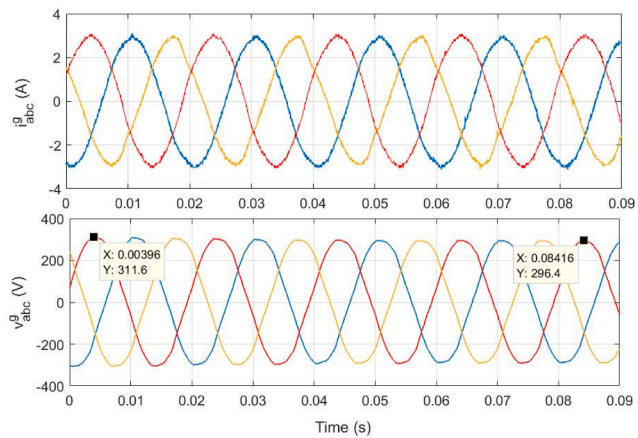


Fig. 27. A 4.8 % symmetrical grid voltage dip occurs at  $t = 0.01$  s. The currents follow their references without any offset.

nominal value. In addition, the performance of the controller against the voltage dip was tested in both the simulation and the experiment, and the robustness against the disturbance with the frequency at around the LCL filter resonance was verified in the simulation.

Also, the controller tracked the reference changes with an acceptable overshoot and settling time. Finally, as the optimization of GPC is performed offline, low real-time computation is needed and the control law can be implemented in a low-cost microcontroller.

**CRedit authorship contribution statement**

**Hasan Zamani:** Conceptualization, Methodology, Software,

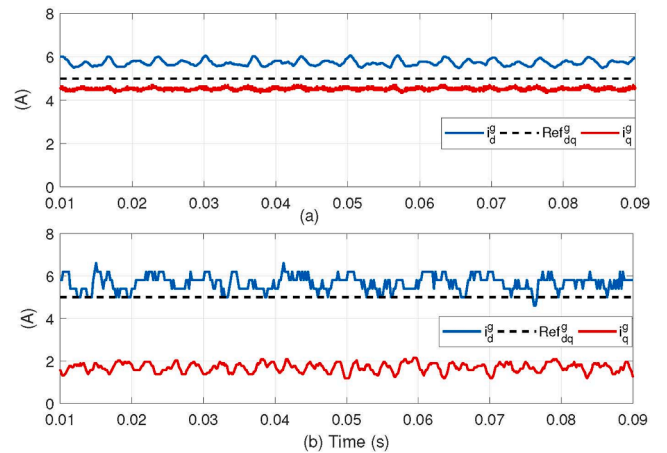


Fig. 28. The dq axes currents (a) without considering the reference trajectory over the interval  $N$ , (b) without considering the reference trajectory and the grid voltage feed-forward term.

Validation, Writing – review & editing. **Karim Abbaszadeh:** Supervision, Writing – review & editing. **MohammadHadi Karimi:** Conceptualization, Methodology, Software, Writing – review & editing. **Johan Gyselinck:** Supervision, Writing – review & editing.

**Declaration of Competing Interest**

The authors declare that they have no known competing financial interests or personal relationships that could have appeared to influence the work reported in this paper.

**Data availability**

No data was used for the research described in the article.

**References**

- [1] Ben Said-Romdhane M, Naouar MW, Slama-Belkhdja I, Monmasson E. Robust active damping methods for LCL filter-based grid-connected converters. *IEEE Trans Power Electron* 2017;32(9):6739–50.
- [2] Gomes CC, Cupertino AF, Pereira HA. Damping techniques for grid-connected voltage source converters based on LCL filter: An overview. *Renew Sustain Energy Rev* 2018;81:116–35.
- [3] Peña-Alzola R, Liserre M, Blaabjerg F, Sebastián R, Dannehl J, Fuchs FW. Analysis of the passive damping losses in LCL-filter-based grid converters. *IEEE Trans Power Electron* 2013;28(6):2642–6.
- [4] Samanes J, Urtasun A, Gubia E, Petri A. Robust multisampled capacitor voltage active damping for grid-connected power converters. *Int J Electr Power Energy Syst* 2019;105:741–52.
- [5] Vieira RP, Martins LT, Massing JR, Stefanello M. Sliding mode controller in a multiloop framework for a grid-connected VSI with LCL filter. *IEEE Trans Ind Electron* 2018;65(6):4714–23.
- [6] Guzman R, de Vicuna LG, Castilla M, Miret J, Martin H. Variable structure control in natural frame for three-phase grid-connected inverters with LCL filter. *IEEE Trans Power Electron* 2018;33(5):4512–22.
- [7] Jiang W, Ma W, Wang J, Wang L, Gao Y. Deadbeat control based on current predictive calibration for grid-connected converter under unbalanced grid voltage. *IEEE Trans Ind Electron* 2017;64(7):5479–91.
- [8] Busada CA, Jorge SG, Solsona JA. Full-state feedback equivalent controller for active damping in LCL-filtered grid-connected inverters using a reduced number of sensors. *IEEE Trans Ind Electron* 2015;62(10):5993–6002.
- [9] Karamanakos P, Mattila R, Geyer T. Fixed switching frequency direct model predictive control based on output current gradients. *IECON 2018–44th Annual Conference of the IEEE Industrial Electronics Society. IEEE*; 2018.
- [10] Piotr, Falkowski. “Finite control set model predictive control for grid-connected NPC Converter with LCL filter and novel resonance damping method.” 2017 19th European Conference on Power Electronics and Applications (EPE’17 ECCE Europe). *IEEE*, 2017.
- [11] Aguilera RP, Lezana P, Quevedo DE. Finite-control-set model predictive control with improved steady-state performance. *IEEE Trans Ind Inf* 2012;9(2):658–67.
- [12] Mohapatra SR, Agarwal V. Model predictive controller with reduced complexity for grid-tied multilevel inverters. *IEEE Trans Ind Electron* 2018;66(11):8851–5.

- [13] Moon J-W, Gwon J-S, Park J-W, Kang D-W, Kim J-M. Model predictive control with a reduced number of considered states in a modular multilevel converter for HVDC system. *IEEE Trans Power Delivery* 2015;30(2):608–17.
- [14] Vatani M, Bahrani B, Saeedifard M, Hovd M. Indirect finite control set model predictive control of modular multilevel converters. *IEEE Trans Smart Grid* 2015;6(3):1520–9.
- [15] Chen X, Wu W, Gao N, Chung H-H, Liserre M, Blaabjerg F. Finite control set model predictive control for LCL-filtered grid-tied inverter with minimum sensors. *IEEE Trans Ind Electron* 2020;67(12):9980–90.
- [16] Karamanakos P, Nahalparvari M, Geyer T. Fixed switching frequency direct model predictive control with continuous and discontinuous modulation for grid-tied converters with LCL filters. *IEEE Trans Control Syst Technol* 2020;29(4):1503–18.
- [17] Garcia CE, Prett DM, Morari M. Model predictive control: Theory and practice—A survey. *Automatica* 1989;25(3):335–48.
- [18] Judewicz MG, Gonzalez SA, Echeverria NI, Fischer JR, Carrica DO. Generalized predictive current control (GPCC) for grid-tie three-phase inverters. *IEEE Trans Ind Electron* 2016;63(7):4475–84.
- [19] Judewicz MG, Gonzalez SA, Fischer JR, Martinez JF, Carrica DO. “Inverter-side current control of grid-connected voltage source inverters with LCL filter based on generalized predictive control.” *IEEE Journal of Emerging and Selected Topics in Power. Electronics* 2018;6(4):1732–43.
- [20] Guzman R, de Vicuna LG, Camacho A, Miret J, Rey JM. Receding-horizon model-predictive control for a three-phase VSI with an LCL filter. *IEEE Trans Ind Electron* 2019;66(9):6671–80.
- [21] Guzman R, de Vicuna LG, Castilla M, Miret J, de la Hoz J. Variable structure control for three-phase LCL-filtered inverters using a reduced converter model. *IEEE Trans Ind Electron* 2018;65(1):5–15.
- [22] Chen Q, Luo X, Zhang L, Quan S. “Model predictive control for three-phase four-leg grid-tied inverters.” *IEEE. Access* 2017;5:2834–41.
- [23] Xue C, Ding Li, Li YunweiRyan. CCS-MPC with long predictive horizon for grid-connected current source converter. 2020 IEEE Energy Conversion Congress and Exposition (ECCE). IEEE; 2020.
- [24] Limon D, Alamo T, de la Peña DM, Zeilinger MN, Jones CN, Pereira M. MPC for tracking periodic reference signals. *IFAC Proceedings Volumes* 2012;45(17):490–5.
- [25] Wang, Liuping, and J. Anthony Rossiter. “Disturbance rejection and set-point tracking of sinusoidal signals using generalized predictive control.” 2008 47th IEEE Conference on Decision and Control. IEEE, 2008.
- [26] Nam NN, Nguyen ND, Yoon C, Choi M, Lee YI. Voltage sensorless model predictive control for a grid-connected inverter with LCL filter. *IEEE Trans Ind Electron* 2022; 69(1):740–51.
- [27] Lim CS, et al. Long horizon linear MPC of grid-connected VSIs: Regulation problems and a plug-in solution. 2017 IEEE Energy Conversion Congress and Exposition (ECCE). IEEE; 2017.
- [28] Jia Y, Zhao J, Xiaowei Fu. Direct grid current control of LCL-filtered grid-connected inverter mitigating grid voltage disturbance. *IEEE Trans Power Electron* 2013;29(3):1532–41.
- [29] Zmood DN, Holmes DG, Bode G. Frequency domain analysis of three phase linear current regulators. Conference Record of the 1999 IEEE Industry Applications Conference Thirty-Forth IAS Annual Meeting (Cat 1999;No. 99CH36370). Vol. 2.
- [30] Camacho EF, Alba CB. Model predictive control. Springer science & business media; 2013.
- [31] Nasiri MR, Farhangi S, Rodriguez J. Model predictive control of a multilevel CHB STATCOM in wind farm application using diophantine equations. *IEEE Trans Ind Electron* 2018;66(2):1213–23.
- [32] Dannehl J, Wessels C, Fuchs FW. Limitations of voltage-oriented PI current control of grid-connected PWM rectifiers with LCL filters. *IEEE Trans Ind Electron* 2008;56(2):380–8.
- [33] Pan D, Ruan X, Bao C, Li W, Wang X. Capacitor-current-feedback active damping with reduced computation delay for improving robustness of LCL-type grid-connected inverter. *IEEE Trans Power Electron* 2014;29(7):3414–27.
- [34] Liu T, Liu J, Liu Z, Liu Z. A study of virtual resistor-based active damping alternatives for LCL resonance in grid-connected voltage source inverters. *IEEE Trans Power Electron* 2020;35(1):247–62.